

Structural and Electrochemical Insights into novel Wadsley Roth Nb₇Ti_{1.5}Mo_{1.5}O₂₅ and Ta₇Ti_{1.5}Mo_{1.5}O₂₅ anodes for Li-ion Battery Application

Green, Alex; Driscoll, Lizzie; Lakhdar, Yazid; Kendrick, Emma; Slater, Peter

DOI:
[10.1039/D3DT02144K](https://doi.org/10.1039/D3DT02144K)

License:
Creative Commons: Attribution (CC BY)

Document Version
Peer reviewed version

Citation for published version (Harvard):
Green, A, Driscoll, L, Lakhdar, Y, Kendrick, E & Slater, P 2023, 'Structural and Electrochemical Insights into novel Wadsley Roth Nb₇Ti_{1.5}Mo_{1.5}O₂₅ and Ta₇Ti_{1.5}Mo_{1.5}O₂₅ anodes for Li-ion Battery Application', *Dalton Transactions*. <https://doi.org/10.1039/D3DT02144K>

[Link to publication on Research at Birmingham portal](#)

General rights

Unless a licence is specified above, all rights (including copyright and moral rights) in this document are retained by the authors and/or the copyright holders. The express permission of the copyright holder must be obtained for any use of this material other than for purposes permitted by law.

- Users may freely distribute the URL that is used to identify this publication.
- Users may download and/or print one copy of the publication from the University of Birmingham research portal for the purpose of private study or non-commercial research.
- User may use extracts from the document in line with the concept of 'fair dealing' under the Copyright, Designs and Patents Act 1988 (?)
- Users may not further distribute the material nor use it for the purposes of commercial gain.

Where a licence is displayed above, please note the terms and conditions of the licence govern your use of this document.

When citing, please reference the published version.

Take down policy

While the University of Birmingham exercises care and attention in making items available there are rare occasions when an item has been uploaded in error or has been deemed to be commercially or otherwise sensitive.

If you believe that this is the case for this document, please contact UBIRA@lists.bham.ac.uk providing details and we will remove access to the work immediately and investigate.

Dalton Transactions

An international journal of inorganic chemistry

Accepted Manuscript

This article can be cited before page numbers have been issued, to do this please use: A. green, E. H. Driscoll, Y. Lakhdar, E. Kendrick and P. R. Slater, *Dalton Trans.*, 2023, DOI: 10.1039/D3DT02144K.



This is an Accepted Manuscript, which has been through the Royal Society of Chemistry peer review process and has been accepted for publication.

Accepted Manuscripts are published online shortly after acceptance, before technical editing, formatting and proof reading. Using this free service, authors can make their results available to the community, in citable form, before we publish the edited article. We will replace this Accepted Manuscript with the edited and formatted Advance Article as soon as it is available.

You can find more information about Accepted Manuscripts in the [Information for Authors](#).

Please note that technical editing may introduce minor changes to the text and/or graphics, which may alter content. The journal's standard [Terms & Conditions](#) and the [Ethical guidelines](#) still apply. In no event shall the Royal Society of Chemistry be held responsible for any errors or omissions in this Accepted Manuscript or any consequences arising from the use of any information it contains.

Structural and Electrochemical Insights into novel Wadsley

Roth $\text{Nb}_7\text{Ti}_{1.5}\text{Mo}_{1.5}\text{O}_{25}$ and $\text{Ta}_7\text{Ti}_{1.5}\text{Mo}_{1.5}\text{O}_{25}$ anodes for Li-ion

Battery Application

A. J. Green^{*1}, E. H. Driscoll², Y. Lakhdar², E. Kendrick², P. R. Slater^{*1}¹School of Chemistry, University of Birmingham, Edgbaston, Birmingham, B15 2TT, UK²School of Metallurgy and Materials, University of Birmingham, Edgbaston, Birmingham, B15 2SE,
UK

Correspondence to:

Alex Green/Prof. Peter Slater

School of Chemistry,

The University of Birmingham,

Edgbaston,

B15 2TT,

UK.



Abstract

View Article Online
DOI: 10.1039/D3DT02144K

Niobium based anodes are gaining increasing popularity for application in high-power lithium-ion batteries, due to their high theoretical capacities, inherent safety at high current densities, and long-term stability. Here, we report the discovery and characterisation of a new Wadsley Roth niobate system, $\text{Nb}_7\text{Ti}_{1.5}\text{Mo}_{1.5}\text{O}_{25}$, showing that it is isostructural with known systems: $\text{Nb}_9\text{PO}_{25}$ and $\text{Nb}_9\text{VO}_{25}$. To evaluate the material's electrochemical performance, including performance at high current densities (for potential high power applications), and long-term stability, Li half-coin cells were prepared. The material showed an initial capacity of 268 (9) mA h g^{-1} at 0.01 A g^{-1} (voltage range of 2.5 – 1.0 V). However, in subsequent cycles, some of this initial capacity is lost, which is attributed to Li trapping associated with the presence of reducible MoO_4 units, similar to the situation observed for isostructural $\text{Nb}_9\text{VO}_{25}$. After this initial irreversible capacity loss, the material showed good performance at high current density rates, such that at 2 A g^{-1} and 4 A g^{-1} respective capacities of 132 (10) mA h g^{-1} and 115 (14) mA h g^{-1} were delivered. Moreover, the material showed respectable capacity retention (97%) after being cycled for 100 cycles at 0.2 A g^{-1} . In order to identify the different Nb, Ti, Mo redox couples involved in this system, a Ta analogue was also synthesized ($\text{Ta}_7\text{Ti}_{1.5}\text{Mo}_{1.5}\text{O}_{25}$) and the electrochemical performance for this phase is also reported. This phase shows a lower initial capacity at 0.01 A g^{-1} (140 (3) mA h g^{-1}) than the Nb analogue in the same voltage range, which can be increased (225 mA h g^{-1}) if a lower cutoff voltage (0.5 V) is applied. The capacity retention for this Ta system after 100 cycles at 0.2 A g^{-1} is similar to the Nb analogue (97 %). Further work has explored whether the Nb-Ti-Mo contents could be varied, and these results showed that single phase $\text{Nb}_{10-2x}\text{Ti}_x\text{Mo}_x\text{O}_{25}$ samples could be prepared for $1.5 \leq x \leq 1.75$, and electrochemical testing results for the $x = 1.75$ endmember are also reported. Overall, this research highlights the synthesis and electrochemical characterisation of two new Wadsley Roth phases, and further highlights the challenges associated with the presence of reducible cations in tetrahedral sites in such structures with respect to minimising initial irreversible capacity loss.

Keywords

Niobium Oxide, High power, Wadsley Roth, Anodes, Li-ion batteries.



Open Access Article. Published on 31 August 2023. Downloaded on 8/31/2023 4:04:29 PM.
This article is licensed under a Creative Commons Attribution 3.0 Unported Licence.



Introduction

View Article Online
DOI: 10.1039/D3DT02144K

With the target of meeting Net Zero in the coming decade, interest in Li-ion battery (LiB) technology has increased substantially, due to their applications in technologies to limit emissions with respect to energy infrastructure. As a prerequisite for commercialization, LiBs need to be safe, cheap, have long lifetimes, and operate at high capacities.¹⁻⁵ To date, graphite (**Figure 1**) is the typical anode of choice and fulfils a large proportion of commercialization requirements (cheap, long-life and a high theoretical capacity of 372 mA h g⁻¹)⁶, but is limited to low (dis)charging rates due to inherent safety implications associated with the formation of lithium dendrites at high charge/discharge rates.⁷ Fast charging and discharging are essential in high-power applications such as power tools, drones, battery powered fork lifts, mining trucks, and rail transport. Li₄Ti₅O₁₂ (175 mA h g⁻¹; LTO)⁸ spinel (**Figure 1**) is a suitable alternative to graphite, which offers a fast-charging solution. However, while this material has favourable attributes in terms of safety and rate capability (the higher operating voltage (1.5 V vs Li/Li⁺) removes the risk of Li dendrite formation)⁹, it leads to a lower energy density for the overall battery compared to a graphite anode cell.

A strategy to improve the energy density for high power application can be found in the use of Wadsley-Roth block structure materials, such as the titanium-doped niobium oxide materials, e.g. TiNb₂O₇ (TNO), Ti₂Nb₁₀O₂₉ and TiNb₂₄O₆₂.¹⁰⁻¹⁵ The dual electron redox ability of the niobium cation, with not only the Nb⁵⁺/Nb⁴⁺ redox couple but a further reduction to Nb³⁺, coupled with the single redox of Ti⁴⁺, allows the theoretical gravimetric capacities to be greatly enhanced, while the operating voltage window of the niobium-based systems is comparable to LTO, thus avoiding Li dendrite formation issues.¹⁸ However, these systems suffer from low electronic conductivity. This issue can potentially be mitigated if oxygen vacancies are introduced into these systems along with carbon encapsulation as identified by Liu *et al.* in a study of a Nb₁₂O_{29-x}/C system.¹⁶ These systems have attracted considerable recent interest, with a wide range of compositions studied, with additional recent examples reported for W-doped niobate and Mo-doped niobate systems including: Nb₁₂WO₃₃,¹⁷ Nb₁₆W₅O₅₅,¹⁸ MoNb₁₂O₃₃^{19,20}, and (W_{0.2}V_{0.8})₃O₇.²¹ In addition to oxide materials work has also been done on heterogeneous transition metal selenide systems (FeSe₂/CoSe₂ and CoSe₂/SnSe₂) which provide high capacities and cycle stability at high rates (4 A g⁻¹).^{22,23}



These Wadsley-Roth structures can be classed as oxygen-deficient derivatives of the ReO_3 crystal structure, containing blocks of corner-linked octahedra, where the oxygen deficiency is accommodated by crystallographic shear planes, in addition to tetrahedral cations in some systems. The corner linked blocks of distorted octahedra are translated in one dimension making $(n \times m)$ networks of MO_6 octahedra with n and m denoting the length and width of the block.²⁴ At the end of these blocks a crystallographic shear plane is created by edge-sharing octahedra,^{25,26} and these crystallographic shear planes help to stabilise the structure by preventing excessive volume expansion on lithiation, thus limiting the degradation of the anode material.^{27, 28,29} The block size in these structures is highly dependent on the metal-to-oxygen ratio, and a higher number of oxygens per metal allows more connections between the corner-sharing octahedra resulting in more substantial block sizes.²⁹ As noted above, the Wadsley-Roth structures are not limited to solely metal octahedra geometry, and in some cases tetrahedral metal sites are also observed.²⁴ Examples of compounds with such tetrahedral sites include $\text{H-Nb}_2\text{O}_5$ and $\text{Nb}_9\text{PO}_{25}$.³⁰⁻³³ The former Nb_2O_5 material has multiple polymorphs, which are not limited to the Wadsley-Roth structure, and have been discussed in detail from a structural and electrochemical perspective by Griffiths *et al.*³⁴

Of direct relevance to the work reported in this paper is $\text{Nb}_9\text{PO}_{25}$. This phase was initially investigated by Roth and co-workers in 1965 and shown to be a (3×3) block structure consisting of NbO_6 octahedra and PO_4 tetrahedra (**Figure 1**).^{30,31} In 2002 Patoux *et al.* conducted lithium insertion studies and concluded that in $\text{Nb}_9\text{PO}_{25}$ there was an approximate 10 % volume expansion during lithiation, with a reported intercalation of 13.5 Li ions per formula unit - and a capacity of 210 mA h g^{-1} .³⁵ The related compound $\text{Nb}_9\text{VO}_{25}$ is isostructural to $\text{Nb}_9\text{PO}_{25}$, with the tetrahedral sites being VO_4 .³⁶⁻³⁸ The main difference with respect to their electrochemical performance, resides with the significant first cycle loss of the V-analogue, attributed to irreversible reduction of V^{5+} to V^{3+} which limits the subsequent lithium intercalation.^{35,39} In 1983 Cava *et al.* investigated the lithium insertion mechanisms associated with these Wadsley-Roth type structures.²⁶ The Li inserts into cavity sites within the block structure, and it has been proposed that the crystallographic shear planes in these systems help to stabilize the structure and prevent octahedral tilt distortions from occurring, thus maintaining open pathways for fast lithium diffusion. Cava and co-workers identified clear trends between 12 Wadsley-Roth structures and their electronic structure and phase



evolution during (de)lithiation.²⁶ The voltage profiles for these Wadsley-Roth shear structures can be split up into 3 sections. The first region is a solid solution with a sloping profile, the second being a two-phase like region with a flatter voltage profile. Depending on the structure this region can be almost flat, like in $\text{H-Nb}_2\text{O}_5$, or have a slight slope (TiNb_2O_7).³⁴ The third region is a solid solution similar to the first region.²⁹

As part of an investigation into new Nb_2O_5 based anode materials, we investigated the substitution of equal amounts of Ti and Mo into Nb_2O_5 leading to the identification of a novel Nb-Ti-Mo-O material, which is isostructural to $\text{Nb}_9\text{PO}_{25}$ and $\text{Nb}_9\text{VO}_{25}$. Initial experiments showed single phase samples for the composition $\text{Nb}_7\text{Ti}_{1.5}\text{Mo}_{1.5}\text{O}_{25}$ (NTMO71515), and here we report the characterisation of this material and the related Ta-analogue ($\text{Ta}_7\text{Ti}_{1.5}\text{Mo}_{1.5}\text{O}_{25}$; TTMO71515).

Through subsequent work on the more technologically interesting Nb system, we illustrate that the phase has a small solid solution range, which can be written as $\text{Nb}_{10-2x}\text{Ti}_x\text{Mo}_x\text{O}_{25}$ ($1.5 \leq x \leq 1.75$).

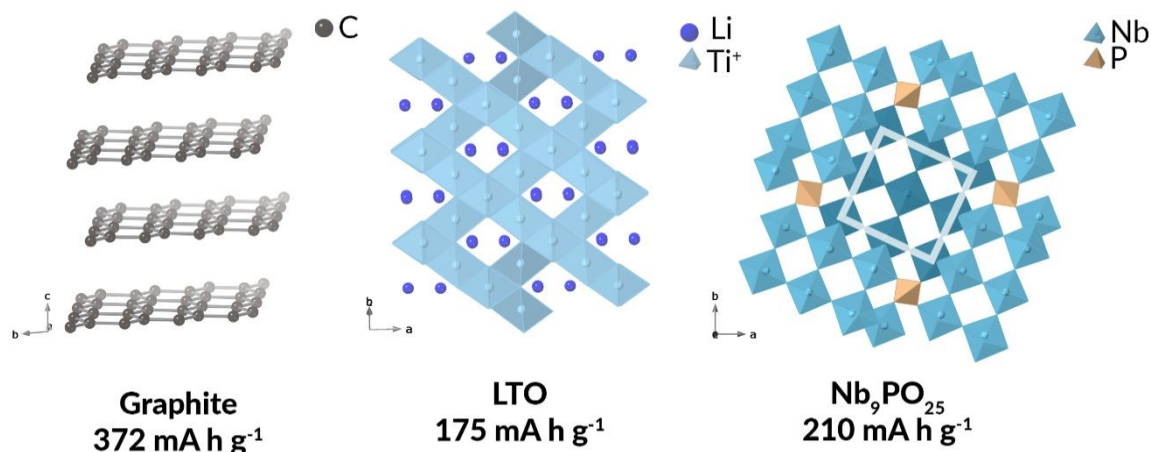


Figure 1: Crystal structures of graphite (left), LTO (middle), and Wadsley-Roth $\text{Nb}_9\text{PO}_{25}$ block (3×3 block highlighted) structure (right).



Experimental

Synthesis and Characterisation

$\text{Nb}_7\text{Ti}_{1.5}\text{Mo}_{1.5}\text{O}_{25}$ (NTMO71515) and $\text{Ta}_7\text{Ti}_{1.5}\text{Mo}_{1.5}\text{O}_{25}$ (TTMO71515) were prepared using the standard solid-state method. Stoichiometric amounts of Nb_2O_5 (Alfa Aesar, 99.5 %), Ta_2O_5 (Alfa Aesar, 99 %), MoO_3 (Alfa Aesar, 99.95 %), and TiO_2 (Anatase; Alfa Aesar) were weighed out and ground together in an agate pestle and mortar, before heating in an alumina crucible at 900 °C for 12 hours under air. The samples were reground and reheated for a further 12 hours at 900 °C under air. Further experiments investigated whether a solid solution range, $\text{Nb}_{10-2x}\text{Ti}_x\text{Mo}_x\text{O}_{25}$, was possible, and x values between $1.25 \leq x \leq 2$ were investigated.

Phase purity was confirmed by powder X-ray diffraction (PXRD) using a Bruker D2 diffractometer between 15 - 70° 2 θ (Co K α). For structure determination, data were collected between 5 - 120° 2 θ on a PANalytical Empyrean diffractometer (Cu K α) for 4 hours, with Rietveld refinements conducted using GSAS II.

Raman spectra were collected using a Renishaw inVia Raman microscope with a 532 nm laser line of 1 % power, involving 10 seconds of exposure and data accumulated over five times, in the range of 50 - 1500 cm^{-1} .⁴¹

Scanning electron microscopy (SEM) images were collected on a Hitachi TM4000 plus tabletop microscope using back scattering electrons at a magnification of x1500 and 5kV.

Coating and Cell Fabrication

The electrode ink coating was prepared with an Active Material (AM): Carbon black (CB): Binder (B) ratio of 80:10:10 using a Thinky Mixer. The binder - polyvinylidene difluoride (PVDF) - was mixed with N-methyl pyrrolidone (NMP) initially for 5 mins/1300 rpm, before additions of the SuperP carbon black and the active material, with subsequent additions of NMP to produce a slurry (10 mins/1300 rpm for each step). To degas the mixture, a final mix of 3 mins/1800 rpm was performed. The resulting slurry was cast onto copper foil using a draw-down coater, where the bar height was set to 200 μm . The resulting coating was dried for up to 2 hours at 80°C before being transferred for overnight drying in a vacuum oven pre-set at 110°C. The coatings were then calendered between 2 stainless steel rollers at 80 °C until the porosity of the coated material was approximately between 30 - 40 %.



The Li-half cells were fabricated in an Ar filled glovebox. Initially, circular disks of the coated active material were cut out (12 mm) and weighed outside the glovebox before being transferred inside. Steel 2032 cases were used, with a single 1 mm stainless steel spacer for compression. The lithium metal electrode was prepared from a dispensed fraction of lithium ribbon, where the surface was scratched using a stainless steel spatula (to remove the tarnished surface and to leave a shiny and rough texture) before being cut to size (12.7 mm) ready for assembly. The electrolyte was 1.0 M LiPF₆ in 50:50 (v/v) ethylene carbonate and dimethyl carbonate – two 50 μL additions were made during assembly. The glass fibre separator was cut to size (14.3 mm).

Electrochemical Testing

The electrochemical performances of the materials were evaluated using a BioLogic BCS805 battery tester, with the cells cycled between 1.0 – 2.5 V in galvanostatic mode. A lower voltage limit of 1.0 V is used instead of 0.01 V (as applied for graphite electrodes) to avoid the potential for Li dendrite formation, as well excessive side reactions caused by the formation of an SEI layer which will lead to lithium inventory loss. Furthermore, the use of such a larger voltage (2.5-0.01 V) window is undesirable for cell manufacturers, as it would lead to a consequent wider full cell voltage range. All cells had formation cycling applied with a current density of 0.01 A g⁻¹ between the two voltage limits. A constant voltage step was applied on lithiation, where the lower voltage limit (1 V) was held for 3 hours or until the current rate decayed to 40% of the value originally applied. A rest of 10 minutes between each cycle was also incorporated.

The rate studies for these materials were performed asymmetrically such that on lithiation a current density of 0.1 A g⁻¹ was consistently applied with the constant voltage step (with 40% current decay limit). The delithiation rate was gradually increased from 0.1 to 4 A g⁻¹ with 5 cycles at each step. Asymmetric cycling was introduced to reduce the current rate limitations created by the use of Li metal in an organic electrolyte.²⁰ After the rate study, five further cycles were conducted at 0.1 A g⁻¹. Following the observation of a higher capacity on returning to 0.1 A g⁻¹, a further test with a modified formation cycle was conducted to see if we could improve the initial capacities of these systems. This formation cycle involved 3 cycles at 0.01 A g⁻¹, 5 cycles at 0.1 A g⁻¹ and finally 10 cycles at 2 A g⁻¹.



For each measurement, three cells were tested under the same conditions, to deduce the average of the (de)lithiation capacities and the associated error in the values (given in parentheses in the text).

A further lower voltage test was performed for TTMO71515 using a BioLogic BCS805 battery tester, with the cell being cycled between 0.5 – 2.5 V in galvanostatic mode. 3 formation cycles were done at a current density of 0.01 A g^{-1} for this test.

Long-term cycling for NTMO71515 and TTMO71515 was performed using a BioLogic BCS805 battery tester, with the cell being cycled between 1 – 2.5 V in galvanostatic mode. 100 cycles at 0.2 A g^{-1} were performed for each cell.



Results and Discussion

View Article Online
DOI: 10.1039/D3DT02144K

Both materials $\text{Nb}_7\text{Ti}_{1.5}\text{Mo}_{1.5}\text{O}_{25}$ (NTMO71515) and $\text{Ta}_7\text{Ti}_{1.5}\text{Mo}_{1.5}\text{O}_{25}$ (TTMO71515) were initially characterised with PXRD. The results showed an XRD pattern similar to the related systems, $\text{Nb}_9\text{PO}_{25}$ and $\text{Nb}_9\text{VO}_{25}$ (tetragonal; space group $I\bar{4}$) as shown in **Figure 2**. The structures were refined using the structure of $\text{Nb}_9\text{PO}_{25}$ as a starting model, with the Rietveld refinement fit shown in **Figure 3** for NTMO71515 and the resulting cell parameters given in **Table 1**.

To aid understanding of the doping strategy from the structural perspective, the original crystal model used in this refinement ($\text{Nb}_9\text{PO}_{25}$) has been included (**Figure 4**). This consists of a (3 x 3) block structure along with tetrahedral sites, with the 4 different crystallographic sites labelled sites 1-4. Site 1 is the corner-sharing tetrahedra which is occupied by P^{5+} for $\text{Nb}_9\text{PO}_{25}$, while sites 2-4 represent different octahedral sites: site 2, the corner-sharing octahedra in the centre of the 3 x 3 block, and sites 3 and 4 the edge-sharing octahedra.

Due to the presence of multiple cations, including isoelectronic Nb^{5+} and Mo^{6+} , and low X-ray scattering of the oxygen, the refinement was conducted in stages – with the starting point involving all octahedral cation sites (site 2-4) set to Nb^{5+} , with Mo^{6+} occupying the tetrahedral site (due to the known greater preference of Mo^{6+} for tetrahedral coordination). Sites which showed low Nb^{5+} content (site 4) were then assumed to be occupied by some Ti^{4+} . Ti^{4+} was then added to all the octahedral and tetrahedral sites and refined. Due to Nb^{5+} and Mo^{6+} being isoelectronic it was not possible to refine individual Nb and Mo occupancies and it is assumed that the Nb^{5+} octahedral sites also contain some Mo^{6+} to match the formula of the material. In order, to confirm the preferred occupancy of Mo^{6+} in the tetrahedral sites, the structure of the equivalent Ta system was also refined (Rietveld refinement profile shown in the supporting information (**SI figure 1**)). Here the significantly different scattering factors of Mo^{6+} and Ta^{5+} allowed the confirmation of the preference for Mo^{6+} in the tetrahedral site. The structural parameters for both systems are tabulated in the Supporting Information (**SI Table 1-2**).

The morphology of both systems was investigated by SEM (**SI Figure 2-3**) and found to exhibit rod-like character.



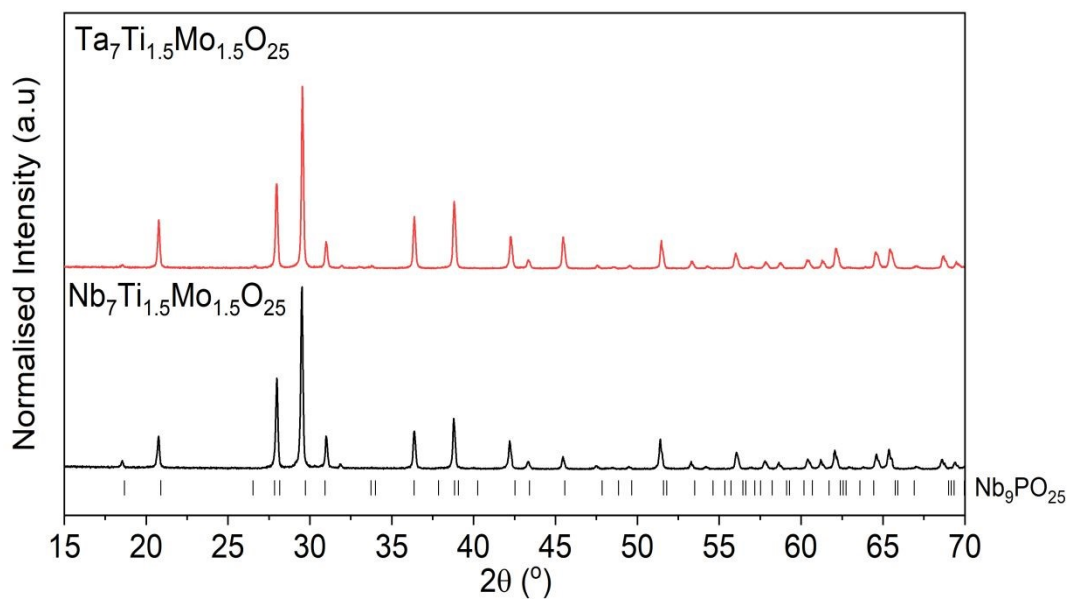


Figure 2: PXRD patterns of NTMO71515 (black) and TTMO71515 (red) Co K α . The peak positions for the isostructural Nb₉PO₂₅ phase are also shown (black dashes).

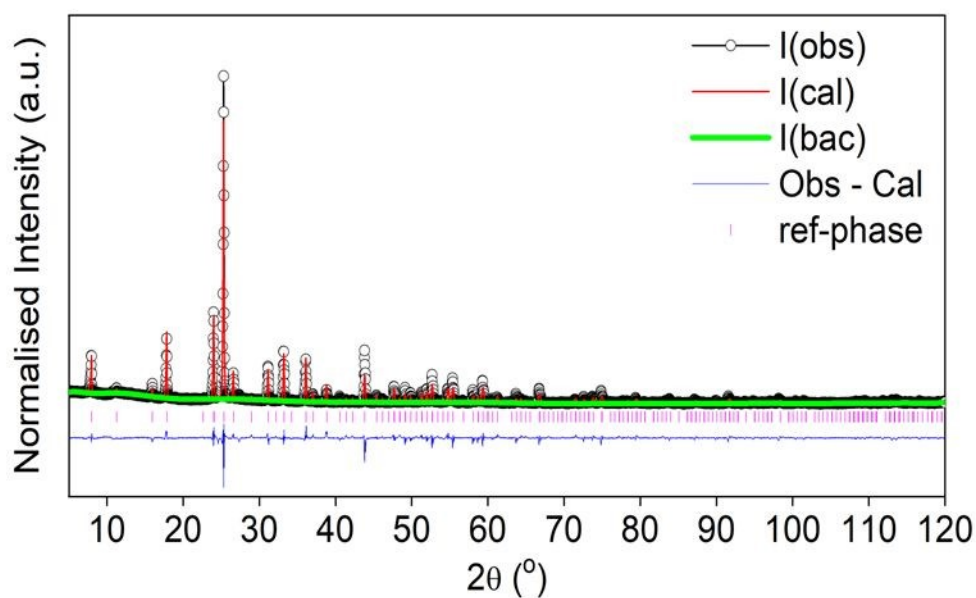


Figure 3: Observed, calculated and difference XRD profiles for NTMO71515 ($R_{wp} - 5.72\%$, $R_p - 3.59\%$) (Cu K α) from Rietveld refinement.



Table 1: Unit cell parameters of $Nb_7Ti_{1.5}Mo_{1.5}O_{25}$ (NTMO71515) and $Ta_7Ti_{1.5}Mo_{1.5}O_{25}$ (TTMO71515).

Material	a (Å)	c (Å)	Volume (Å ³)	R _{wp} (%)
NTMO71515	15.6879(3)	3.8031(1)	936.00(4)	5.72
TTMO71515	15.6587(3)	3.8043(7)	932.80(3)	9.51

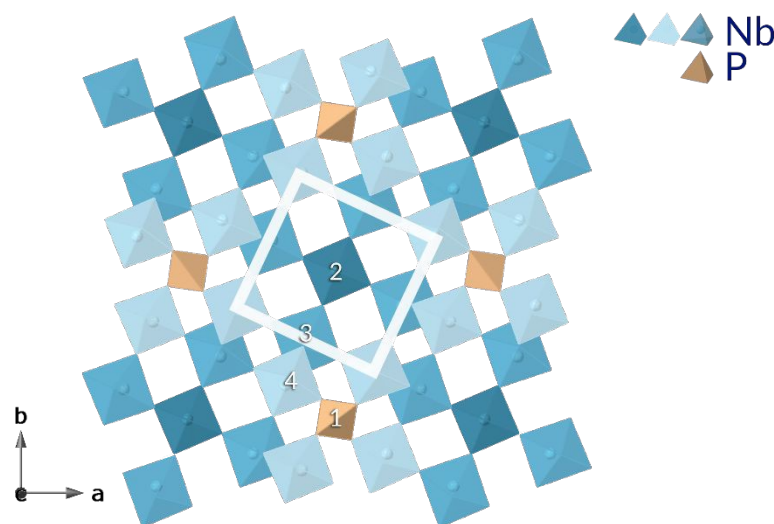


Figure 4: Crystal structure of the Nb_9PO_{25} system. There are 4 crystallographic sites in the structure. Site 1 is the tetrahedral cation site (orange). Site 2 is the centre octahedra of the 3 x 3 block (dark blue). Site 3 (blue) and 4 (light blue) are the edge-sharing octahedra.

Raman spectra were recorded for both samples, as shown in **Figure 5**, to further evaluate the bonding in these materials. The spectra show that at wavenumbers below 150 cm^{-1} , the peaks for the Ta-analogue are shifted to lower wavenumbers compared to the Nb material, with the most intense Raman mode being at 128 cm^{-1} and 112 cm^{-1} for the Nb and Ta phases, respectively. At wavenumbers greater than 150 cm^{-1} , the opposite occurs, as the Raman peaks for the Ta-analogue are shifted to higher wavenumbers. Previous work by Perfler *et al.*, comparing $TiNb_2O_7$ and $TiTa_2O_7$, observed similar trends.⁴² By comparison with this past literature, the symmetric metal-oxygen stretching modes for the corner and edge-sharing



TaO₆/NbO₆ octahedra can be assigned to the 1008 cm⁻¹ peak (Ta phase), and 992 cm⁻¹ peak (Nb phase). The peaks at 932 cm⁻¹ (Ta) and 918 cm⁻¹ (Nb) are likely due to a combination metal-oxygen stretching modes from the TaO₆/NbO₆ octahedra and MoO₄ tetrahedra.⁴³ The shifts in the Raman bands to higher wavenumbers for the Ta phase can be attributed to the higher bond strengths and force constants of the Ta-O bonds compared to the Nb-O bonds, with the vibrational modes predominantly involving vibrations of the O atoms, with the metal at the centre of the octahedra not moving⁴² For the lower wavenumber region (below 150 cm⁻¹) the bands can be attributed to O-(Nb/Ta)-O symmetric and antisymmetric bending vibrations, that predominantly involve vibrations of the Nb/Ta atoms (the increase in mass for Ta at the centre of the MO₆ octahedra leading to a shift to lower wavenumber).⁴⁴ Similar to this previous study comparing TiNb₂O₇ and TiTa₂O₇, the bands situated between the wavenumbers 550-700 cm⁻¹ can be attributed to the Ti-O stretching modes.⁴²

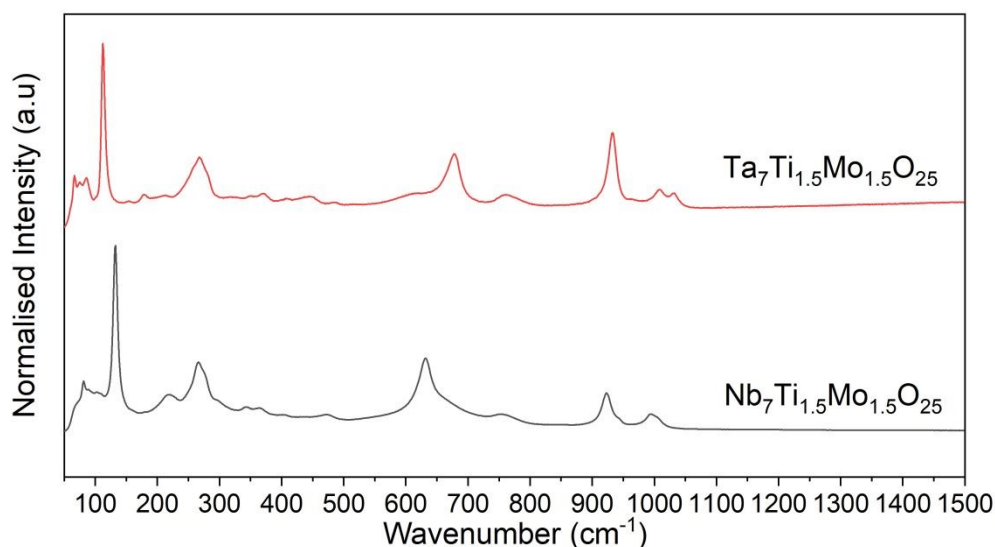


Figure 5: Raman spectra of NTMO71515 (black) and TTMO71515 (red).

Electrochemical Performance

The compounds have 3 redox active elements Nb/Ta, Ti, Mo where Nb⁵⁺/Ta⁵⁺ might be expected to reduce to 4+/3+, Ti⁴⁺ to Ti³⁺ and Mo⁶⁺ to Mo⁴⁺. Assuming complete reduction to Nb³⁺/Ta³⁺, Ti³⁺, Mo⁴⁺, 18.5 Li would be intercalated into the systems which would give theoretical capacities for NTMO71515 (RMM: 1,266 g mol⁻¹) and TTMO71515 (RMM: 1,882 g



mol⁻¹) of 391 and 263 mA h g⁻¹, respectively. The charge-discharge voltage profiles for NTMO71515 and TTMO71515 on formation cycling (at current density of 0.01 A g⁻¹) are presented in **Figure 6**. The initial discharge capacity for NTMO71515 was found to be 268 (9) mA h g⁻¹ which correlates to ca. 12.7 moles of electrons (lithium insertion) in the process, with the lower capacity attributed with only partial reduction of Nb to 3+, similarly to observed previously for other Wadsley Roth phases. The second cycle shows a 37 mA h g⁻¹ capacity loss (1.7 Li⁺ irreversibly trapped) with a returned discharge capacity of 231 (17) mA h g⁻¹. For the TTMO71515 system the capacity for the first discharge was found to be 140 (3) mA h g⁻¹ corresponding to lower level of Li incorporation under the same conditions, ca. 9.8 moles of electrons (lithium insertion), suggesting a significantly reduced level of Ta reduction compared to Nb. The second cycle shows a discharge capacity of 98 (4) mA h g⁻¹, corresponding to a loss of 2.9 Li⁺, which is greater than observed for NTMO71515. A breakdown of all the capacities associated with different voltage windows for all 3 formation cycles is provided in the supplementary information (**SI Table 3-4**) along with voltage profile comparisons between NTMO71515 and TTMO71515 (**SI Figure 4-6**).

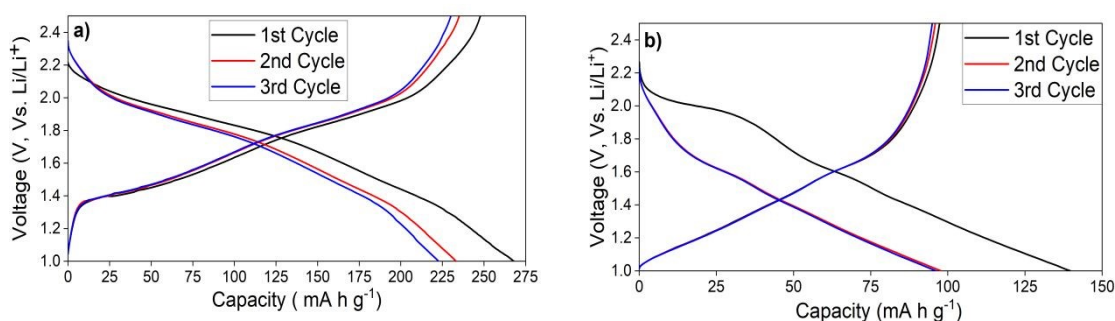


Figure 6: Galvanostatic discharge-charge curves of NTMO71515 (a) and TTMO71515 (b), vs. Li metal, with a current density of 0.01 A g⁻¹ applied.

To understand the chemistry and the redox couples at play during (de)lithiation, the differential scanning calorimetry (dQ/dV) were plotted (**Figure 7**). For the NTMO71515 system, three reversible peaks and one irreversible peak can be observed in the dQ/dV plot. The irreversible peak located at 2.20 V is attributed to the Mo reduction process in the tetrahedral sites. The irreversible redox contributes to a drop in capacity, which is attributed to Li being trapped by this irreversible Mo reduction. The isostructural phase, Nb₉VO₂₅, has a similar significant decrease in capacity due to the irreversible reduction of V in the tetrahedral sites.^{45,46} At 1.90 V a reversible peak is observed corresponding to the overlapping redox



couples of Mo^{6+} - Mo^{4+} (oct sites), Ti^{4+} - Ti^{3+} and Nb^{5+} - Nb^{4+} and the peak at 1.42 V can be attributed as the partial Nb^{4+} - Nb^{3+} redox peak.^{20,47,48} The dQ/dV plot for NTMO71515 shows no clear shifting of the peaks between the first and third cycle. However, the intensities do decrease slightly between the first and second cycle highlighting the loss of Li during the first cycle.²⁰ **SI Figure 9** shows a large decrease in peak intensities and shifting of the peaks in the dQ/dV plot between the formation cycles at 0.01 A g^{-1} and the start of the rate test at 0.1 A g^{-1} , which correlates with the further significant decrease in capacity we observe between these 2 rates.

In order to provide further support for the above assignments, the dQ/dV plots for the Ta-analogue were measured, which show similarities to NTMO71515. For TTMO71515 three reversible and one irreversible redox peak can be observed. Like NTMO71515 the irreversible redox peak at 1.94 V is assigned to the tetrahedral Mo site redox process (shifted to lower V for the Ta analogue) whilst the Mo^{6+} - Mo^{4+} (oct site) shows one peak at 1.62 V.^{50,51} The dQ/dV plot shows a reversible peak at 1.42 V which is attributed as the Ti^{4+} - Ti^{3+} redox process. The third reversible peak at 1.12 V is attributed to the Ta^{5+} - Ta^{4+} partial redox process. Comparisons between the dQ/dV plots for NTMO71515 and TTMO71515 can be seen in **SI Figure 7-9**. The dQ/dV plot for TTMO71515 shows a similar decrease in peak intensities to the NTMO71515 system which we also accredit to the irreversible loss in Li between the first and second cycle due to Li trapping. There is a clear shift in all the redox peak positions to lower voltages compared to the Nb analogue, illustrating a significant influence on the overall redox processes on changing from Nb to Ta. Given the observed shift in the redox peaks to lower voltages for the Ta analogue, a further analysis of the Ta sample was performed to a lower voltage, 0.5 – 2.5 V, at a current density of 0.01 A g^{-1} for 3 cycles (**SI Figure 10**). A breakdown of all the capacities associated with different voltage windows for all 3 cycles is provided in the supplementary information (**SI Table 5**). This study confirmed that there is Ta redox below 1 V as the capacity increased from 140 (3) mA h g^{-1} when the voltage limit was 1 V to 225 mA h g^{-1} for the 0.5 V cut-off. The resulting dQ/dV plot also highlights further Ta reversible redox around 1 V (**SI Figure 11**).



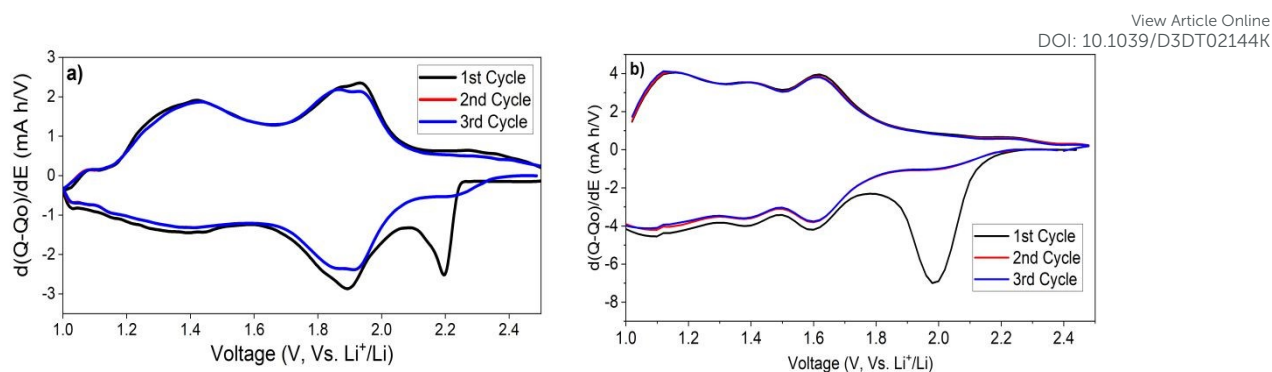


Figure 7: Differential scanning calorimetry (dQ/dV) plot derived from the galvanostatic discharge/charge profile of NTMO71515 (a) and TTMO71515 (b), vs. Li metal at a rate corresponding to 0.01 A g^{-1} .

To test the electrochemical rate performance and capacity retention of NTMO71515 and TTMO71515, additional measurements were performed at varying current densities ($0.1 - 4 \text{ A g}^{-1}$) using asymmetric cycling conditions ($1 - 2.5 \text{ V}$ window), where the lithiation rate was kept constant at 0.1 A g^{-1} whilst the delithiation rate was gradually increased. The resulting gravimetric capacity at each rate for NTMO71515 is shown in **Figure 8**. While there is an initial drop in capacity on cycling from 0.01 to 0.1 A g^{-1} (values of 220 (19) and 151 (12) mA h g^{-1} obtained respectively), subsequent retention at higher rates is good, with the average capacity found to be 132 (10) and 115 (14) mA h g^{-1} , for the rates of 2 A g^{-1} and 4 A g^{-1} respectively (corresponding to ca. 7.5C and 15C respectively). The capacity retention over the 5 cycles for each rate does not drop below 98% and there is only a 13% loss in capacity between current densities of 0.1 and 2 A g^{-1} (151 (12) – 132 (10) mA h g^{-1}). Even between 0.1 and 4 A g^{-1} (151 (12) – 115 (14) mA h g^{-1}) there is only a 27% decrease in capacity highlighting the good rate capability of this system. **SI Table 6** shows the average capacity retention at different current densities and the associated C- rate for NTMO71515. Upon completing the rate study with a final 5 cycles at 0.1 A g^{-1} , interestingly the capacity recovered to 160 (11) mA h g^{-1} , which is higher than its original value at the start of the rate study (151 (12) A h g^{-1}) – thus suggesting the original formation process needs to be further optimised in these systems, and thus may offer further potential to enhance performance, and that the high delithiation rates applied did not negatively impact the material. Long-term cycling was performed on this NTMO71515 material which confirmed good capacity retention on extended cycling (**SI Figure 12**). For this study, 100 cycles at a current density of 0.2 A g^{-1} were



performed and a 97% retention in capacity was delivered emphasising the good cycle life of this system.

To investigate the increase in capacity at lower current density rates when fast cycling is performed, we prepared additional cells where we added extra formation cycling at higher rates - 3 cycles at 0.01 A g^{-1} , 5 cycles at 0.1 A g^{-1} and finally 10 cycles at 2 A g^{-1} . This revised formation cycling was tested, and the results can be seen in **SI Figure 15**. The results show that the capacity of the material at 0.1 A g^{-1} can be slightly enhanced from $149 (1) \text{ mA h g}^{-1}$ to $156 (1) \text{ mA h g}^{-1}$ if a faster rate (2 A g^{-1}) is applied in the formation cycle. This increase in capacity suggests that further study of formation protocols is warranted for Wadsley Roth phases, such as these.

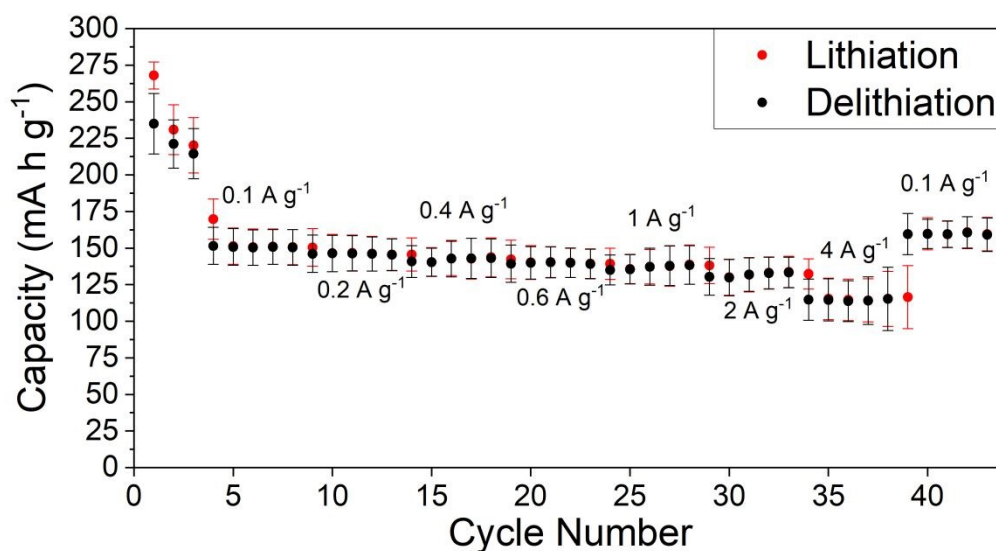


Figure 8: Average specific capacities of three NTMO71515 cells undergoing asymmetric cycling – such that the lithiation current density is maintained at 0.1 A g^{-1} , while the delithiation gradually increases after 5 cycles at each rate step. The red error bars are for lithiation, the black ones are for the delithiation.

TTMO71515 was also shown to display good capacity retention, after the initial decrease seen for the current densities between 0.01 and 0.1 A g^{-1} ($95 (2) - 79 (3) \text{ mA h g}^{-1}$), corresponding to a 18 % reduction in capacity. Subsequently the capacity only decreased from $79 (2) \text{ mA h g}^{-1}$ to $60 (1) \text{ mA h g}^{-1}$ for the wide range of current densities from $0.1 - 4 \text{ A g}^{-1}$ (27 % drop in capacity) with the capacity retention over 5 cycles at each rate staying above 99% (**Figure 9**). **SI Table 7** shows the average capacity retention at different current densities and the



associated C- rate for TTMO71515. However, the Ta-analogue exhibits lower gravimetric capacities, due to its high relative molecular mass and lack of Ta redox activity above 1 V – thus making it a poorer anode material compared to the Nb analogue in the range 2.5-1.0 V. Moreover Ta is significantly higher in cost than Nb, which is another negative attribute. Long-term cycling was also performed for this system for 100 cycles at 0.2 A g⁻¹. The capacity dropped from 89 mA h g⁻¹ to 86 mA h g⁻¹ over 100 cycles showcasing a similar 97 % capacity retention observed as for NTMO71515 (SI Figure 13).

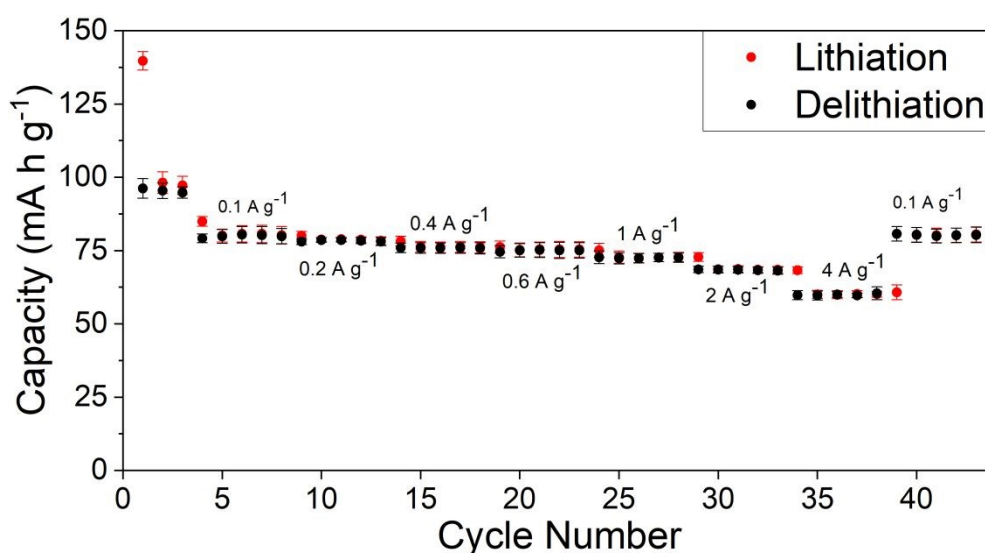


Figure 9: Average specific capacities of three TTMO71515 cells undergoing asymmetric cycling – such that the lithiation current density is maintained at 0.1 A g⁻¹, while the delithiation gradually increases after 5 cycles at each rate step. The red error bars are for lithiation, black are for the delithiation.

Investigation of solid solution range for the Nb-Ti-Mo-O system

In order to investigate whether these were line phases, or exhibited a solid solution range, (see Figure 10, with cell parameters given in Table 2), albeit the impurities were small for x=2 (SI Figure 14).



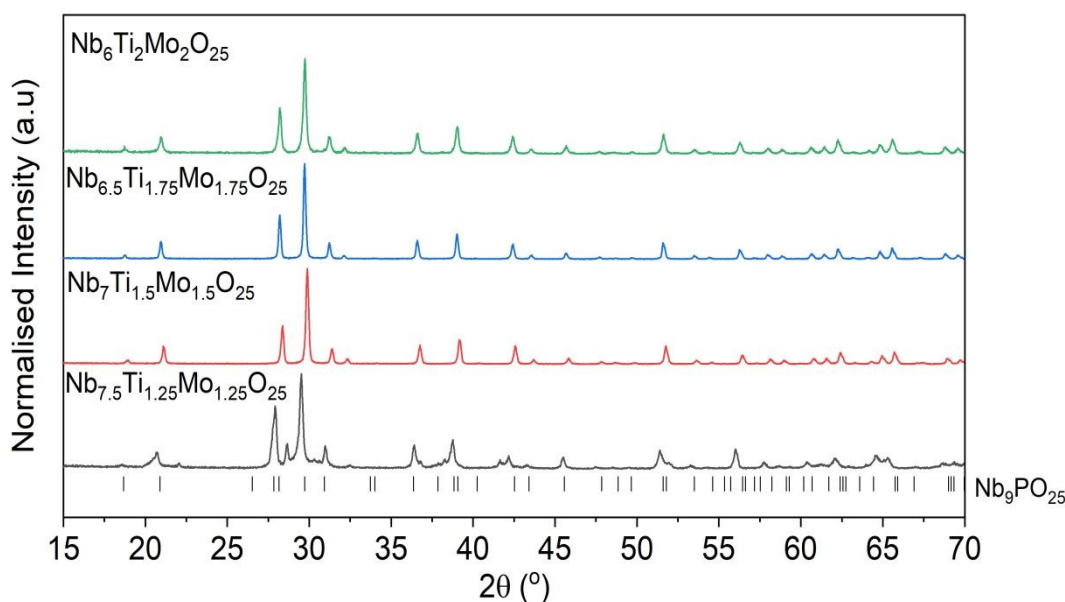


Figure 10: XRD patterns of the solid solution $Nb_{10-2x}Ti_xMo_xO_{25}$ ($1.25 \leq x \leq 2$). Nb_9PO_{25} phase tick marks (black dashes) are also shown.

Table 2: Unit cell parameters of NTMO71515 and NTMO65175175.

Material	a (Å)	c (Å)	Volume (Å ³)
NTMO71515	15.6879(3)	3.8031(1)	936.00(4)
NTMO65175175	15.6853(2)	3.8015(3)	935.28(3)

The electrochemical performance of the $x = 1.75$ endmember of the solid solution series was also investigated (**Figure 11**). The electrochemical performance showed a higher initial capacity (290 (4) mA h g⁻¹) along with an accompanying higher first cycle loss (19%) than NTMO71515, with a decrease to 234 (4) mA h g⁻¹ in the second cycle, which is most likely related to the higher Mo content. After the initial losses, NTMO65175175 has good capacity retention for rates between 0.1 – 2 A g⁻¹ with the capacity retention over 5 cycles at each rate staying above 99%. However, at faster rates (4 A g⁻¹) the retention falls off to 89%, with the capacity fading from 118 (2) to 106 (1) mA h g⁻¹. Upon completing the rate study with a final 5 cycles at 0.1 A g⁻¹, the lithiation capacity recovered to 158 (7) mA h g⁻¹ compared to 170 (5) mA h g⁻¹ for the first set of cycles at 0.1 A g⁻¹. This decrease in capacity suggests this higher Mo content material does not recover as well as NTMO71515 after being cycled at higher



current densities. **SI Table 8** shows the average capacity retention at different current densities and the associated C- rate for NTMO65175175.

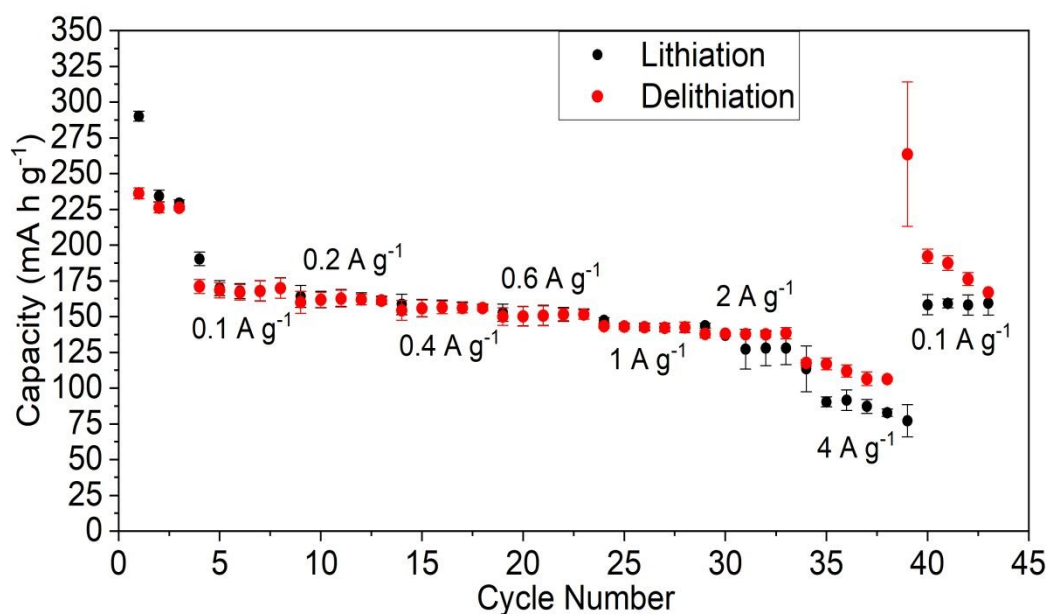


Figure 11: Average specific capacities of two NTMO65175175 cells undergoing asymmetric cycling – such that the lithiation current density is maintained at 0.1 A g^{-1} , while the delithiation gradually increases after 5 cycles at each rate step. The red error bars are for lithiation, black are for the delithiation.

Conclusions

In conclusion, we have reported the synthesis and characterisation of the new Wadsley Roth phases $\text{Nb}_7\text{Ti}_{1.5}\text{Mo}_{1.5}\text{O}_{25}$ (NTMO71515) and $\text{Ta}_7\text{Ti}_{1.5}\text{Mo}_{1.5}\text{O}_{25}$ (TTMO71515), which are isostructural with $\text{Nb}_9\text{PO}_{25}/\text{Nb}_9\text{VO}_{25}$. From electrochemical testing within a Li-half coin cell, NTMO71515 shows high capacity for first cycle of $268 (9) \text{ mA h g}^{-1}$ ($2.5 - 1.0 \text{ V}$), which decreases significantly over the initial few cycles, attributed to Li trapping mediated by irreversible reduction of Mo in the tetrahedral sites (similar to prior results for $\text{Nb}_9\text{VO}_{25}$). Despite the initial capacity lost, this material shows subsequent good capacity retention at increasing rates between 0.1 and 2 A g^{-1} with the capacity only dropping from 152 mA h g^{-1} to 133 mA h g^{-1} over this range– equivalent to a 13 % drop. Furthermore, the capacity recovers to above its original values when the lower current density 0.1 A g^{-1} is re-applied, suggesting further optimisation is required for the formation cycling to maximise values, while also showing that the material is unaffected by high rate cycling. Further studies showed that this phase can also be prepared containing higher Ti/Mo contents, with a solid solution range



observed; $\text{Nb}_{10-2x}\text{Ti}_x\text{Mo}_x\text{O}_{25}$ ($1.5 \leq x \leq 1.75$). The Ta analogue phase, TTMO71515, showed lower capacities, attributed both to the heavier mass and the reduced Ta redox in the 1.0 – 2.5 V voltage window. However, the comparison of the data for this phase and NTMO71515 allowed confirmation of the Mo preference for the tetrahedral site and helped in the assignment of the redox couples at play in both materials.

View Article Online
DOI: 10.1039/D3DT02144K

Author Contributions

Alex J. Green: Investigation, data curation, formal analysis, visualization, writing – original draft, writing – review and editing.

Elizabeth H. Driscoll: Methodology, visualization, writing – original draft, and writing – review and editing.

Yazid Lakhdar: Methodology – review and editing.

Emma Kendrick: Supervision, resources, and writing – review and editing.

Peter R. Slater: Conceptualization, methodology, supervision, resources, writing – original draft, and writing – review and editing.

Acknowledgements

We would like to thank Faraday Institution: FITG045 (AJG studentship), CATMAT (FIRG016), and ReLiB (FIRG027) projects for funding.

Conflict of Interest

There are no conflicts to declare.



References

View Article Online
DOI: 10.1039/D3DT02144K

- 1 L. Suo, F. Han, X. Fan, H. Liu, K. Xu and C. Wang, *J. Mater. Chem. A*, 2016, **4**, 6639–6644.
- 2 T. Tsujikawa, K. Yabuta, T. Matsushita, T. Matsushima, K. Hayashi and M. Arakawa, *J. Power Sources*, 2009, **189**, 429–434.
- 3 L. K. K. Maia, L. Drünert, F. La Mantia and E. Zondervan, *J. Clean. Prod.*, 2019, **225**, 928–938.
- 4 C. P. Grey and D. S. Hall, *Nat. Commun.*, 2020, **11**, 6279.
- 5 D. Deng, *Energy Sci. Eng.*, 2015, **3**, 385–418.
- 6 H. Zhang, Y. Yang, D. Ren, L. Wang and X. He, *Energy Storage Mater.*, 2021, **36**, 147–170.
- 7 X. Xu, S. Wang, H. Wang, C. Hu, Y. Jin, J. Liu and H. Yan, *J. Energy Chem.*, 2018, **27**, 513–527.
- 8 E. Ferg, R. J. Gummow, A. de Kock and M. M. Thackeray, *J. Electrochem. Soc.*, 1994, **141**, 147–150.
- 9 M. M. Thackeray and K. Amine, *Nat. Energy*, 2021, **6**, 683.
- 10 C. Yang, S. Deng, C. Lin, S. Lin, Y. Chen, J. Li and H. Wu, *Nanoscale*, 2016, **8**, 18792–18799.
- 11 X. Wu, J. Miao, W. Han, Y.-S. Hu, D. Chen, J.-S. Lee, J. Kim and L. Chen, *Electrochem. Commun.*, 2012, **25**, 39–42.
- 12 H. Aghamohammadi, N. Hassanzadeh and R. Eslami-Farsani, *J. Alloys Compd.*, 2022, **911**, 165117.
- 13 J.-T. Han, Y.-H. Huang and J. B. Goodenough, *Chem. Mater.*, 2011, **23**, 2027–2029.
- 14 T. Jiang, S. Ma, J. Deng, T. Yuan, C. Lin and M. Liu, *Adv. Sci.*, 2022, **9**, 2105119.
- 15 O. A. Drozhzhin, V. V. Grigoryev, A. M. Alekseeva, R. R. Samigullin, D. A. Aksyonov, O. V. Boytsova, D. Chernyshov, V. V. Shapovalov, A. A. Guda, A. V. Soldatov, K. J.



- Stevenson, A. M. Abakumov and E. V. Antipov, *ACS Appl. Mater. Interfaces*, 2021, **13**, 56366–56374. View Article Online
DOI: 10.1039/D1DT02144K
- 16 C. Liu, B. Wang, L. Xu, K. Zou, W. Deng, H. Hou, G. Zou and X. Ji, *ACS Appl. Mater. Interfaces*, 2023, **15**, 5387–5398.
- 17 D. Saritha, V. Pralong, U. V. Varadaraju and B. Raveau, *J. Solid State Chem.*, 2010, **183**, 988–993.
- 18 K. J. Griffith, K. M. Wiaderek, G. Cibin, L. E. Marbella and C. P. Grey, *Nature*, 2018, **559**, 556–563.
- 19 X. Zhu, J. Xu, Y. Luo, Q. Fu, G. Liang, L. Luo, Y. Chen, C. Lin and X. S. Zhao, *J. Mater. Chem. A*, 2019, **7**, 6522–6532.
- 20 Y. Lakhdar, H. Geary, M. Houck, D. Gastol, A. S. Groombridge, P. R. Slater and E. Kendrick, *ACS Appl. Energy Mater.*, 2022, **5**, 11229–11240.
- 21 K. E. Wyckoff, D. D. Robertson, M. B. Preefer, S. M. L. Teicher, J. Bienz, L. Kautzsch, T. E. Mates, J. A. Cooley, S. H. Tolbert and R. Seshadri, *Chem. Mater.*, 2020, **32**, 9415–9424.
- 22 S. Tao, R. Momen, Z. Luo, Y. Zhu, X. Xiao, Z. Cao, D. Xiong, W. Deng, Y. Liu, H. Hou, G. Zou and X. Ji, *Small*, 2023, **19**, 2207975.
- 23 S. Tao, J. Cai, Z. Cao, B. Song, W. Deng, Y. Liu, H. Hou, G. Zou and X. Ji, *Adv. Energy Mater.*, 2023, 2301653.
- 24 Y. Yang and J. Zhao, *Adv. Sci.*, 2021, **8**, 202004855.
- 25 B. D. Sten Andersson and D. A. D Wadsley, *Nature*, 1966, **211**, 581–583.
- 26 R. J. Cava, D. W. Murphy and S. M. Zahurak, *J. Electrochem. Soc.*, 1983, **130**, 2345–2351.
- 27 K. J. Griffith, I. D. Seymour, M. A. Hope, M. M. Butala, L. K. Lamontagne, M. B. Preefer, C. P. Koçer, G. Henkelman, A. J. Morris, M. J. Cliffe, S. E. Dutton and C. P. Grey, *J. Am. Chem. Soc.*, 2019, **141**, 16706–16725.
- 28 M. Kunz and I. David Brown, *J. Solid State Chem.*, 1995, **115**, 395–406.



- 29 C. P. Koçer, K. J. Griffith, C. P. Grey and A. J. Morris, *J. Am. Chem. Soc.*, 2019, **141**, 15121–15134. View Article Online
DOI: 10.1039/D3DT02144K
- 30 R. S. Roth, A. D. Wadsley and S. Anderson, *Acta Cryst.*, 1965, **18**, 643–647.
- 31 O. A. Drozhzhin, M. A. Vorotyntsev, S. R. Maduar, N. R. Khasanova, A. M. Abakumov and E. V. Antipov, *Electrochim. Acta*, 2013, **89**, 262–269.
- 32 H. Yu, J. Zhang, R. Zheng, T. Liu, N. Peng, Y. Yuan, Y. Liu, J. Shu and Z.-B. Wang, *Mater. Chem. Front.*, 2020, **4**, 631–637.
- 33 H. Yu, J. Zhang, M. Xia, C. Deng, X. Zhang, R. Zheng, S. Chen, J. Shu and Z.-B. Wang, *J. Mater.*, 2020, **6**, 781–787.
- 34 K. J. Griffith, A. C. Forse, J. M. Griffin and C. P. Grey, *J. Am. Chem. Soc.*, 2016, **138**, 8888–8899.
- 35 S. Patoux, M. Dolle, G. Rouse and C. Masquelier, *J. Electrochem. Soc.*, 2002, **149**, A391–A400.
- 36 M. T. Casais, E. Gutiérrez-Puebla, M. A. Monge, I. Rasines and C. Ruíz-Valero, *J. Solid State Chem.*, 1993, **102**, 261–266.
- 37 C. Jiang, T. Liu, N. Long, X. Cheng, N. Peng, J. Zhang, R. Zheng, H. Yu and J. Shu, *Ceram. Int.*, 2019, **45**, 18111–18114.
- 38 S. Qian, H. Yu, L. Yan, H. Zhu, X. Cheng, Y. Xie, N. Long, M. Shui and J. Shu, *ACS Appl. Mater. Interfaces*, 2017, **9**, 30608–30616.
- 39 J. Xu, S. C. Chen, K. V. Ramanujachary and M. Greenblatt, *Inorg. Chem.*, 1994, **33**, 267–270.
- 40 M. Wang, Z. Yao, Q. Li, Y. Hu, X. Yin, A. Chen, X. Lu, J. Zhang and Y. Zhao, *J. Energy Chem.*, 2022, **69**, 601–611.
- 41 E. H. Driscoll, A. Orera, P. A. Anderson, M. L. Sanjuán and P. R. Slater, *Dalton Trans.*, 2021, **50**, 3315–3323.
- 42 L. Perfler, V. Kahlenberg, C. Wikete, D. Schmidmair, M. Tribus and R. Kaindl, *Inorg. Chem.*, 2015, **54**, 6836–6848.



- 43 J. C. Sczancoski, L. S. Cavalcante, M. R. Joya, J. A. Varela, P. S. Pizani and E. Longo, *Chem. Eng. J.*, 2008, **140**, 632–637. View Article Online
DOI: 10.1039/D3DT02144K
- 44 K. Nakamoto, *Infrared and Raman Spectra of Inorganic and Coordination Compounds: Part A: Theory and Applications in Inorganic Chemistry: Sixth Edition*, 2008, 1–419.
- 45 C. Jiang, T. Liu, N. Long, X. Cheng, N. Peng, J. Zhang, R. Zheng, H. Yu and J. Shu, *Ceram. Inter.*, 2019, **45**, 18111–18114.
- 46 M. Liang, Y. Huang, Y. Lin, G. Liang, C. Huang, L. Chen, J. Li, Q. Feng, C. Lin and Z. Huang, *J. Mater. Sci. Technol.*, 2021, **83**, 66–74.
- 47 J. Cheng, F. Lu and X. Kuang, *Mater. Adv.*, 2021, **2**, 6272–6277.
- 48 R. Tao, T. Zhang, S. Tan, C. J. Jafta, C. Li, J. Liang, X. G. Sun, T. Wang, J. Fan, Z. Lu, C. A. Bridges, X. Suo, C. L. Do-Thanh and S. Dai, *Adv. Energy Mater.*, 2022, **12**, 2200519.
- 49 J.-M. Price, P. Allan and P. Slater, *Energy Adv.*, 2023, **2**, 864–876.
- 50 D. Saritha and U. V. Varadaraju, *Mater. Res. Bull.*, 2013, **48**, 2702–2706.
- 51 Y. N. NuLi, Z. W. Fu, Y. Q. Chu and Q. Z. Qin, *Solid State Ion.*, 2003, **160**, 197–207.

